ACS APPLIED MATERIALS & INTERFACES
Research Article
www.acsami.org

Phase Stability and Stoichiometry in Thin Film Iron Pyrite: Impact on Electronic Transport Properties

Xin Zhang,[†] Tom Scott,[‡] Tyler Socha,[†] David Nielsen,[†] Michael Manno,[†] Melissa Johnson,[†] Yuqi Yan,[†] Yaroslav Losovyj,[‡,§] Peter Dowben,[‡] Eray S. Aydil,*[,†] and Chris Leighton*[,†]

[†]Department of Chemical Engineering and Materials Science, University of Minnesota, Minneapolis, Minnesota 55455, United States
[‡]Department of Physics and Astronomy, University of Nebraska—Lincoln, Lincoln, Nebraska 68588, United States
[§]Department of Chemistry, Indiana University, Bloomington, Indiana 47405, United States

Supporting Information

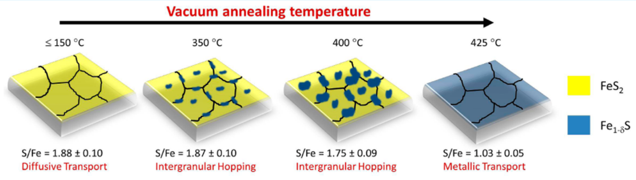

ABSTRACT: The use of pyrite FeS_2 as an earth-abundant, low-cost, nontoxic thin film photovoltaic hinges on improved understanding and control of certain physical and chemical properties. Phase stability, phase purity, stoichiometry, and defects, are central in this respect, as they are frequently implicated in poor solar cell performance. Here, phase-pure polycrystalline pyrite FeS_2 films, synthesized by ex situ sulfidation, are subject to systematic reduction by vacuum annealing (to 550 °C) to assess phase stability, stoichiometry evolution, and their impact on transport. Bulk probes reveal the onset of pyrrhotite ($Fe_{1-\delta}S$) around 400 °C, rapidly evolving into the majority phase by 425 °C. This is supported by X-ray photoelectron spectroscopy on (001) crystals, revealing surface $Fe_{1-\delta}S$ formation as low as 160 °C, with rapid growth near 400 °C. The impact on transport is dramatic, with $Fe_{1-\delta}S$ minority phases leading to a crossover from diffusive transport to hopping (due to conductive $Fe_{1-\delta}S$ nanoregions in an FeS_2 matrix), followed by metallicity when $Fe_{1-\delta}S$ dominates. Notably, the crossover to hopping leads to an inversion of the sign, and a large decrease in magnitude of the Hall coefficient. By tracking resistivity, magnetotransport, magnetization, and structural/chemical parameters vs annealing, we provide a detailed picture of the evolution in properties with stoichiometry. A strong propensity for S-deficient minority phase formation is found, with no wide window where S vacancies control the FeS_2 carrier density. These findings have important implications for FeS_2 solar cell development, emphasizing the need for (a) nanoscale chemical homogeneity, and (b) caution in interpreting carrier types and densities.

KEYWORDS: *photovoltaic devices, pyrite, thin films, phase stability, stoichiometry, charge transport, doping*

1. INTRODUCTION

The pyrite form of FeS_2 has long been recognized as a material with high potential as a solar absorber for photovoltaic devices (see ref 1). This is due to pyrite's exceptional absorption coefficient ($>10^5$ cm^{-1} above 1.2−1.4 eV[1] rendering a less than 100 nm thick-film capable of absorbing over 90% of the sun's light), good mobility (>300 cm^{2}V^{-1}s^{-1} in single crystal form[1]), and a suitable minority carrier diffusion length (100−1000 nm[1]). Nevertheless, a significant research effort from the mid 1980s proved unsuccessful in realizing high performance FeS_2-based solar cell devices.[1] Short circuit current densities >30 mA cm^{-2} were obtained, along with good quantum efficiency, but with open circuit voltages <0.2 V, limiting power conversion efficiencies to under 3%, even in single-crystal-based photoelectrochemical cells.[1] Such disappointing results led to dwindling interest in pyrite as a solar absorber in the 1990s, particularly in light of the emergence of CdTe and Cu(In,Ga)-Se_2 as thin film photovoltaics.[2]

This downturn in interest has recently been reversed in light of the realization that FeS_2 may represent a near ideal choice for a photovoltaic material from economic, toxicity, and earth abundance perspectives.[3] A number of new thin film[4−8] and nanoparticle/nanowire[9−13] synthesis methods have been developed, and an improved understanding of single crystal properties,[14,15] defects,[5,6,11,13−18] doping,[5,6,11,13−18] and surfaces and interfaces[10,14,15,19−22] are being sought. Significantly, a recent publication has reconfirmed the poor performance of pyrite, in a variety of solar cell device architectures,[23] underscoring the need to resolve significant fundamental issues with the physical and chemical properties of FeS_2 before progress can be made.

While no *single* problem underlying the poor photovoltaic performance of pyrite FeS_2 has yet been definitively isolated, a number of potential factors have been identified. There are, for instance, abundant issues with FeS_2 surfaces and interfaces. Conductive surface layers,[1,5,6,10,14,15,24] surface inversion layers,[5,14,15,25] surface electronic states,[1,5,6,10,14,15,24] surface nonstoichiometry, defects, and deep traps,[1,5,10,15,16,20−22] and a reduced surface energy gap[26] have all been discussed. Doping is another contentious issue in pyrite, where, for example, bulk

Received: April 20, 2015
Accepted: June 8, 2015
Published: June 18, 2015

ACS Publications © 2015 American Chemical Society

DOI: 10.1021/acsami.5b03422
ACS Appl. Mater. Interfaces 2015, 7, 14130−14139

single crystals are almost exclusively *n*-type[1,14,27] (perhaps due to S vacancies[14]), whereas polycrystalline thin films are typically deduced to be *p*-type.[1,5,6,10,11,13,28−31] The fundamental reason(s) for this are not understood, and controlled intentional *n*- and *p*-doping of FeS_2 thus remains an outstanding challenge.

Significant in this context is that, of the existing thin film studies, only a small fraction report mobilities sufficiently large that diffusive transport can be safely assumed, and thus Hall measurements simply interpreted. In many other cases, thin film mobilities are so low that interpretation of the Hall coefficient should be explicitly acknowledged as nontrivial. Our recent work with FeS_2 films synthesized by ex situ sulfidation of Fe[32] emphasized this point, showing that low mobility *n*-type films can be easily mistaken for *p*-type, due to the Hall coefficient diminishing, and reversing sign, with the onset of hopping transport. This is a well-known phenomenon in disordered semiconductors, *a*-Si providing the textbook example.[33−35] In our recent report, the specific situation giving rise to nondiffusive transport was found to be hopping associated with nanoscopic Fe-rich clusters in the FeS_2 matrix, at volume fractions far beneath typical X-ray detection limits.[32] While these clusters were eradicated at higher processing temperatures,[32] this nevertheless highlights another issue with pyrite films: the management of nanoscale stoichiometry variations. Also important is the frequently observed low mobility,[1,5,6,11,13,18,32] which seems to be associated with uncontrolled doping at densities up to even 10^{20}−10^{21} cm^{-3},[1,5,6,11,13,18,32] far beyond what can be used in solar cells. Although a number of potential explanations have been advanced, including some ubiquitous uncontrolled dopant,[5,6,17,18] it is unclear what defect(s) is actually responsible.

The issue of (non)stoichiometry arises frequently in the above. Nonstoichiometric defects (both bulk and surface),[1,5,10,15,16,20−22,36] *n*-doping by S vacancies (e.g., ref 14), FeS-like surface layers,[16,21,22] and a strong tendency to form S-deficient bulk impurity phases[16] have all been discussed. S-poor impurity phases are a particular concern with FeS_2 given the stability of FeS (troilite), Fe_7S_8 (pyrrhotite), the related pyrrhotite ordered defect phases in the $Fe_{1-\delta}S$ range, and greigite Fe_3S_4.[37] Additionally, while equilibrium bulk phase diagrams depict FeS_2 as a line-compound with a decomposition temperature of 740 °C, some nonstoichiometry is certainly possible, particularly at semiconductor doping levels,[14,16] as is the onset of surface/bulk decomposition at temperatures well below that shown in the bulk phase diagram, potentially at temperatures relevant to typical processing conditions. Thorough studies of nonstoichiometry and phase stability in pyrite crystals and films are thus timely, particularly if solid connections can be made to electronic properties and doping.

It is in this context that we have performed a systematic study of the structural, chemical, transport, magnetotransport, and magnetic properties of initially phase-pure FeS_2 thin films as a function of vacuum annealing, seeking to understand phase stability, stoichiometry evolution with reduction, and their impact on transport. At annealing temperatures of 400 °C, bulk probes first detect the formation of a pyrrhotite ($Fe_{1-\delta}S$) minority phase. At temperatures only 25 °C higher, this phase becomes dominant in diffraction and Raman spectroscopy, demonstrating an abrupt transformation from pyrite to pyrrhotite. Complementary X-ray photoelectron spectroscopy measurements from the (001) surfaces of FeS_2 single crystals help understand this, surface signatures of $Fe_{1-\delta}S$ being detected at as low as 160 °C, with a rapid increase in phase fraction around 400 °C. This stoichiometry evolution is dramatically reflected in transport, which reveals sequential crossovers from conventional semiconductor transport to hopping (in this case associated with nanoscale conductive clusters of $Fe_{1-\delta}S$ in the FeS_2 matrix), then from hopping to metallic behavior (due to the conductive $Fe_{1-\delta}S$ majority phase). The former crossover is accompanied by a sign reversal and a decrease in the magnitude of the Hall coefficient, again highlighting the difficulties associated with eliminating nanoscale chemical inhomogeneity in pyrite films, and with interpreting the sign of the Hall coefficient.[32] Careful examination of the structural, chemical, transport, and magnetic parameters provides a detailed picture of the conversion from pyrite to pyrrhotite with reduction. A central finding is the absence of a significant window over which reduction of pyrite to $FeS_{2-\delta}$ allows for doping control, at least at these carrier densities, the formation of pyrrhotite minority phases being preferred. Similarly, at least in the absence of significant S vapor pressure, annealing in this temperature range does not seem promising for mitigation of high carrier density and low mobility in these FeS_2 films. As will be discussed in detail, these results have numerous implications for future FeS_2-based solar cell development.

2. RESULTS AND ANALYSIS

As discussed in Section 4 below (Experimental Section), polycrystalline thin film pyrite FeS_2 was synthesized by ex situ sulfidation of Fe. This employed the methods reported in ref 32, essentially 600 °C sulfidation of 33 nm-thick Fe on $Al_2O_3(0001)$ substrates, to yield 110 nm-thick polycrystalline pyrite with grain size ∼100 nm,[32] i.e., a "monolayer" of grains. At such high sulfidation temperatures, the films are phase-pure (marcasite-free) pyrite based on laboratory wide-angle X-ray diffraction (WAXRD) and Raman spectroscopy.[32] Depth-profiled Auger electron spectroscopy measurements reveal a uniform composition profile, albeit with evidence for interdiffusion at the Al_2O_3/FeS_2 interface. Energy dispersive spectroscopy (EDS) puts the S/Fe ratio at 1.88 ± 0.10. Importantly, under these synthesis conditions, hopping conduction due to nanoscale Fe-rich clusters is eradicated, with simple activated transport dominating at low temperature (T).[32] Hall effect measurements unambiguously establish *n*-type conduction, typical room temperature electron density (n), resistivity (ρ), and mobility (μ) lying at 10^{20} to 10^{21} cm^{-3}, 0.1 to 0.01 $cm^2V^{-1}s^{-1}$, and ∼0.5 Ωcm.[32]

2.1. Bulk Structural/Chemical Characterization. Figure 1(a),(b) presents the WAXRD pattern and Raman spectrum from an as-deposited (unannealed) single-phase polycrystalline pyrite FeS_2 film. In this figure, the lower section of panel (a) shows the expected reflections from (cubic) pyrite FeS_2[38] and (monoclinic) pyrrhotite Fe_7S_8,[39] while the lower section of (b) shows the expected Raman peak positions for pyrite FeS_2.[4−6,10,11,13,40] In between the panels, the S/Fe ratio from EDS is listed. Consistent with the above statements, the data from unannealed films suggest phase-pure pyrite FeS_2.

Figure 1(a,b) also shows the evolution in such bulk characterization data with vacuum annealing temperature (T_A), through 550 °C. Up to T_A = 350 °C, the WAXRD and Raman scattering remain essentially unperturbed by annealing, single-phase pyrite FeS_2 being preserved. Consistent with this, the EDS S/Fe ratio is unchanged within experimental uncertainty. A small but distinct change takes place at T_A =

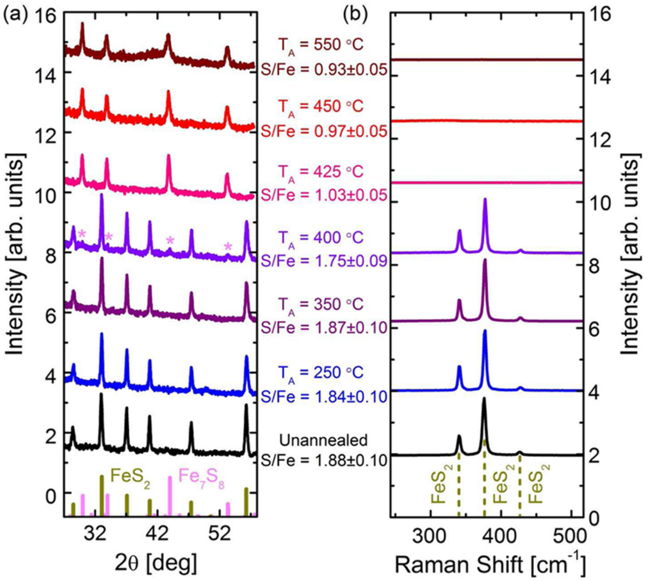

Figure 1. (a) Wide-angle X-ray diffraction from $Al_2O_3(0001)/FeS_2$ films after a 1 h vacuum anneal (1×10^{-6} Torr) at temperatures (T_A) between 250 and 550 °C. An unannealed film is shown for comparison. At the bottom, the green (magneta) lines show the expected pyrite FeS_2 (pyrrhotite Fe_7S_8) powder patterns. For T_A = 400 °C, magneta asterisks mark reflections from pyrrhotite. (b) Raman spectra of the same films. At the bottom, the green dashed lines mark the 344, 380, and 430 cm^{-1} peaks expected from pyrite FeS_2.[40] The pyrrhotite phase dominating at $T_A \geq 425$ °C is Raman inactive in this range.[40] No marcasite FeS_2 (expected peak positions 323, 385, 391, and 441 cm^{-1}) is detected. All plots are vertically displaced by ~2 arbitrary units for clarity. In between the panels, the S/Fe ratio from energy dispersive spectroscopy is labeled.

400 °C, however, where the WAXRD begins to reveal weak reflections associated with polycrystalline pyrrhotite $Fe_{1-\delta}S$, although the Raman scattering remains unchanged. The S/Fe ratio also decreases at this annealing temperature, to 1.75 ± 0.09. Remarkably, further increasing T_A by only 25 °C, to 425 °C, results in complete suppression of Raman scattering in the probed wavenumber range, a transformation in the WAXRD to a pattern consistent with phase-pure polycrystalline $Fe_{1-\delta}S$, and a sharp drop in the S/Fe ratio to 1.03 ± 0.05. The absence of Raman peaks in pyrrhotite is consistent with prior work, which shows that pyrrhotite is Raman inactive in this window.[40] It is important to note at this stage that the WAXRD results in Figure 1(a) are specifically compared to the Fe_7S_8 phase of pyrrhotite. As shown in the Supporting Information (SI, see Figure S1), the WAXRD patterns of the various pyrrhotite $Fe_{1-\delta}S$ phases are, however, similar, particularly for nonzero δ. While no attempt is made to distinguish among them at this stage, additional data presented below will shed more light on this issue. Further increasing T_A to 450 and 550 °C results in little additional change in WAXRD, nothing in Raman, and only a weak decrease in the S/Fe ratio, which falls to 0.93 ± 0.05 at 550 °C. In short, these bulk structural and chemical probes indicate, as a function of T_A, nominally phase-pure pyrite FeS_2 up to 350 °C, the onset of a pyrrhotite $Fe_{1-\delta}S$ minority phase at 400 °C, followed by a rapid transformation to majority phase pyrrhotite by 425 °C. The evolution in S/Fe is consistent with this, within experimental uncertainty.

2.2. Surface Chemical Characterization. To further probe the evolution in phase stability and stoichiometry with vacuum annealing, in particular to obtain higher sensitivity to the onset of pyrrhotite formation, complementary X-ray photoelectron spectroscopy (XPS) was performed as a function of T_A, as described in more detail in Section 4. Given the nature of XPS, which is surface-specific (typically probing no more than the first 2 to 5 unit cells (see the Experimental Section, Section 4, below for more details), and sensitive to crystalline orientation, this aspect of the characterization was performed not on polycrystalline films, but on single crystal FeS_2. As described in more detail in Section 4 below, and following an adaptation of a method previously used for high quality CoS_2,[41] a variant of chemical vapor transport (CVT) was employed to grow the crystals. This resulted in stoichiometric, phase-pure, single crystal pyrite FeS_2 specimens, as verified by WAXRD, Raman, EDS, and X-ray diffraction with a 2D area detector. A summary of the results is provided in the SI (see Figures S2 and S3). The (001) surfaces were identified by crystal habit, verified by X-ray diffraction with a 2D detector, and used for the XPS measurements. In terms of surface preparation, Ar ion sputtering and annealing procedures were found to alter the surface stoichiometry and lower the pyrite $FeS_2(001)$ surface stability (as previously reported[22]), and thus were avoided. The measurements were performed at a photon energy of 1486.6 eV. This is relatively high in comparison to some prior work,[21,22] and thus less sensitive to the extreme surface region.

The S 2*p* core level formed the focus of these XPS studies, as this spectral region provides information on the nature of the bonding with Fe, the nominal Fe valence, and the surface stoichiometry. As shown in Figure 2(a), unannealed pyrite $FeS_2(001)$ single crystal surfaces show the S $2p_{3/2}/2p_{1/2}$ doublet around 162.8 ± 0.2/164.0 ± 0.1 eV in binding energy, with an intensity ratio near 0.5. For reference, prior studies report the S $2p_{3/2}$ core level binding energy as 162.6,[42] 162.9,[43] and 163.1 eV,[44] in good agreement with the results shown here. With increasing T_A up to 380 °C, this S 2*p* doublet gradually shifts to lower binding energies, followed by a clear and abrupt transformation between 380 and 410 °C, where a new S 2*p* doublet at 162.6 ± 0.3 and 161.4 ± 0.2 eV emerges. The spectra then continue to gradually evolve through T_A = 530 °C, resulting by 600 °C in a simple doublet shifted by ~1.3 eV from the FeS_2 starting point (unannealed data). Reference to prior literature confirms that the spectrum at 600 °C is in fact quantitatively similar to prior work on pyrrhotite $Fe_{1-\delta}S$,[22,42,45] and associated by Andersson et al.[22] and Herbert et al.[21] with S vacancies in FeS_2. Between ambient and 600 °C the spectra were thus fit to a four peak model, describing the S $2p_{3/2}$ and $2p_{1/2}$ peaks for both FeS_2 and $Fe_{1-\delta}S$. This process is illustrated for the representative case of T_A = 450 °C in Figure 2(a), showing the four individual peaks in addition to the background (see figure caption for details). These intensities were then used to extract the molar phase fractions of FeS_2 and $Fe_{1-\delta}S$, resulting in the T_A dependence shown in Figure 2(b). Note that the use of S 2*p* core level spectra enables this analysis with no need for corrections due to the energy-dependent electron analyzer transmission function, photoemission cross sections, or mean-free-paths.

As expected from inspection of Figure 2(a), minor amounts of $Fe_{1-\delta}S$ begin to form on the pyrite surface after vacuum annealing at temperatures as low as 160 °C, but with a remarkably rapid increase between 380 and 410 °C. Above this temperature, the pyrrhotite molar fraction steadily increases, reaching about 0.9 by 600 °C. While the important distinctions between surface and bulk sensitivity, and (001) vs. random

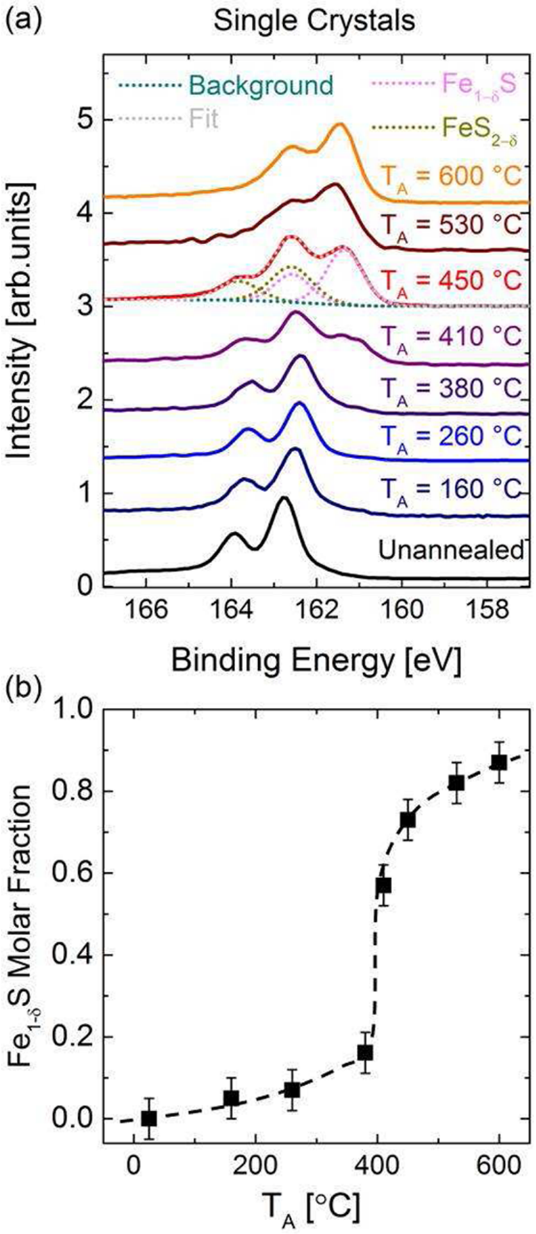

Figure 2. (a) Annealing temperature dependent (160 °C $\le T_A \le$ 600 °C) X-ray photoemission spectra from the S 2p core level on the surface of an $FeS_2(001)$ single crystal. An unannealed crystal is shown for comparison. (b) The molar fraction of $Fe_{1-\delta}S$ [$Fe_{1-\delta}S/(Fe_{1-\delta}S + FeS_{2-\delta})$] vs T_A, as extracted from XPS spectral components. The dashed line is a guide to the eye. The T_A = 450 °C data in (a) show an example of the decomposition into background (blue dotted line), $Fe_{1-\delta}S$ (pink dotted line), and $FeS_{2-\delta}$ (green dotted line) components, resulting in the shown fit (gray dotted line through red data).

orientation, must be kept in mind when comparing Figures 1 and 2, the results are broadly consistent. Minor pyrrhotite formation, likely limited to the surface, occurs at as low as 160 °C in vacuum,[21] followed by far faster conversion to pyrrhotite around 380 °C. In polycrystalline films, the latter is likely initiated at the surface and in the grain boundary regions. By 410 °C, however, the transformation from pyrite FeS_2 to pyrrhotite $Fe_{1-\delta}S$ is substantially complete, and $Fe_{1-\delta}S$ becomes the majority phase. Vacuum annealing at still higher temperatures results in near phase-pure $Fe_{1-\delta}S$.

2.3. Electronic (and Magnetic) Properties.

In order to probe the impact on electronic transport properties of the phase and stoichiometry evolution with vacuum annealing captured in Figures 1 and 2, wide T range $\rho(T)$ measurements were made at various T_A. As shown in Figure 3(a), the unannealed polycrystalline pyrite FeS_2 films have $\rho \approx$ 0.5 Ωcm at 300 K, monotonically increasing to $>10^3$ Ω·cm on cooling to liquid helium temperatures.[32] Vacuum annealing at T_A up to 400 °C results in what *appear* to be only relatively small changes in $\rho(T)$, clear semiconducting-like ($d\rho/dT \ll 0$) behavior being preserved. This is consistent with retention of a pyrite FeS_2 majority phase up to 400 °C, as seen in Figure 1. Between 400 and 425 °C, however, where the structural/

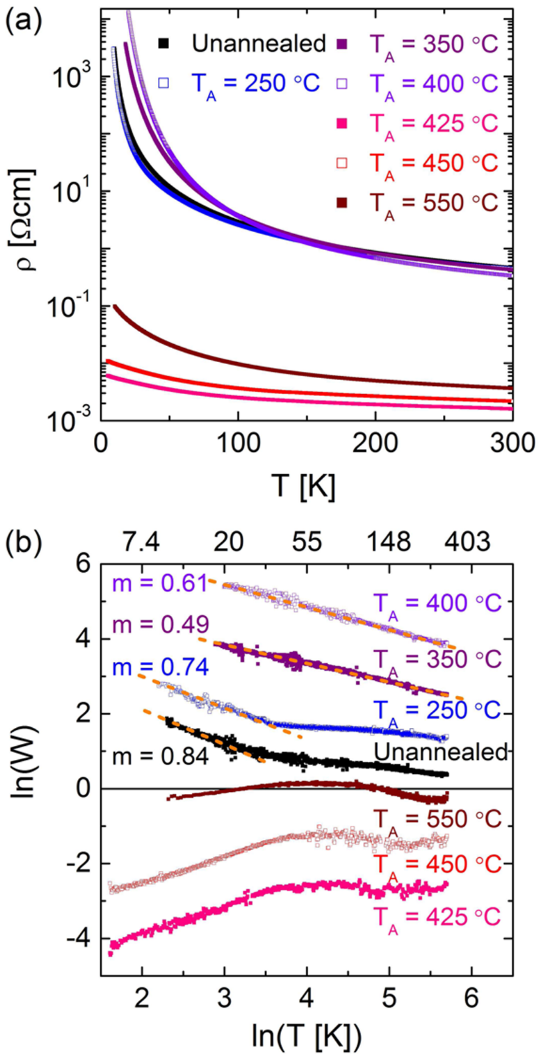

Figure 3. (a) Temperature (T) dependence of the resistivity (ρ) of $Al_2O_3(0001)/FeS_2$ films annealed at temperatures (T_A) between 250 and 550 °C. An unannealed film is also shown. The data are plotted on a log–linear scale. (b) ln$W$ vs ln$T$ for the same films, where $W = -d\ln\rho/d\ln T$. The curves for the unannealed film and the film at T_A = 550 °C have no vertical shifts. The curves at T_A = 250, 350, and 400 °C, whose ln$W$ values are always positive, have been vertically shifted up, while the curves at T_A = 425 and 450 °C, whose ln$W$ values are always negative, have been vertically shifted down, for clarity. For $T_A \le$ 400 °C, straight line low T fits are labeled with the slope m, from $\rho = \rho_0 \exp(T_0/T)^m$. The T_A = 350 and 400 °C curves result in T_0 values of 2650 and 4700 K, respectively.

chemical data (e.g., Figure 1) reveal a sharp transition from a pyrite to pyrrhotite majority phase, the $\rho(T)$ behavior also abruptly alters. The low T resistivity in fact falls by over 6 orders of magnitude between T_A = 400 and 425 °C, the strongly semiconducting behavior at $T_A \leq 400$ °C transitioning to a regime of small negative $d\rho/dT$ and mΩcm resistivities at T_A = 425 °C. This is consistent with the established electronic properties of pyrrhotite $Fe_{1-\delta}S$, which is known to be a good conductor; room temperature ρ is in the 0.1−1 mΩcm range in naturally occurring single crystals.[37,46]

To probe this transformation more deeply, particularly around $T_A \approx 400$ °C where pyrrhotite begins to form as a bulk minority phase, Zabrodskii plots[47] can be used. These are ln$W$ vs ln$T$ plots, where the quantity W, termed the reduced activation energy, is defined as $W = -d\ln\rho/d\ln T$. On such plots ln$W$ decreasing as ln$T$ is lowered is characteristic of conduction on the metallic side of the metal−insulator transition (MIT), whereas ln$W$ increasing as ln$T$ is lowered is indicative of conduction on the insulating side of the MIT. Moreover, if the resistivity on the insulating side of the MIT is of the form $\rho = \rho_0 \exp (T_0/T)^m$, where ρ_0 is the $T \to \infty$ value of the resistivity and T_0 is some characteristic temperature, a ln$W$ vs ln$T$ plot linearizes this form, resulting in a straight line of slope $-m$.[47] This provides a quantitative, unbiased means to extract m, which is indicative of the active transport mechanism. As discussed in our prior work,[32] and in more detail elsewhere,[48,49] $m = 1$ corresponds to simple activated behavior ($\rho = \rho_0 \exp (T_0/T)$), as for conventional thermal activation from some dopant level. Values of m of 1/4 or 1/2 on the other hand (i.e., $\rho = \rho_0 \exp (T_0/T)^{1/4}$ or $\rho = \rho_0 \exp (T_0/T)^{1/2}$, respectively), indicate variable-range hopping (VRH) of either Mott type (constant density-of-states around the Fermi level), or Efros−Shklovkii type (where electron−electron interactions open a soft-gap at the Fermi energy).[48]

As discussed in ref 32, in an *inhomogeneous* semiconductor, an alternative explanation for $m = 1/2$ is possible, associated with conductive clusters in a more insulating matrix. Specifically, if these clusters are sufficiently small (nanoscopic), the Coulombic energy penalty associated with charging a cluster with a single hopping electron ($e^2/4\pi\varepsilon d$, where e is the electronic charge, ε is the dielectric constant, and d is the cluster diameter) becomes significant, resulting in "granular metallic conduction". Early modeling of this situation by Abeles, Sheng, and co-workers[50,51] ascribed the conduction to hopping between conductive clusters, which they argued results in $\rho = \rho_0 \exp (T_0/T)^{1/2}$. Their derivation, however, relied on a specific assumption regarding the ratio of d to the intercluster separation.[50,51] This assumption was later criticized by a number of authors, on both experimental and theoretical grounds.[52−54] Zhang and Shklovskii thus advanced an alternative picture where doping in the insulating matrix leads to random charging of the conductive clusters, and finite density-of-states at the Fermi level.[53] This density-of-states is soft- rather than hard-gapped, recovering Efros−Shklovskii $\rho = \rho_0 \exp (T_0/T)^{1/2}$ behavior.[53] For the current paper, the essential point is that detection of $m = 1/2$ *can* indicate conventional Efros−Shklovskii VRH in a homogeneous semiconductor, but can also result from conductive nanoregions in a more insulating matrix. The latter was in fact directly implicated in our prior work on ex situ sulfidized FeS_2 films, where sulfidation temperatures below the 600 °C used here resulted in nanoscopic unreacted Fe-rich clusters.[32]

To directly determine m in the current case, where the electronic transport is controlled by the vacuum annealing temperature, T_A, Figure 3(b) plots ln$W$ vs ln$T$ for the films shown in Figure 3(a). As expected,[32] the unannealed FeS_2 film has $m = 0.84$ at low T, the proximity to unity indicating close to simple activated transport. (As discussed in full in ref 32, strict adherence to simple activated behavior over a broad T range is not seen in these FeS_2 films; further mitigation of the high doping density and low mobility will be needed to obtain truly diffusive transport). As T_A is increased to 250 °C, this behavior is largely unchanged, although m falls slightly to 0.74.

At 350 and 400 °C, the situation is remarkably different, which is not obvious from direct inspection of Figure 3(a). At these T_A values, not only does ln$W$ become linear in ln$T$ over an exceptionally wide T range (from ambient to liquid helium temperatures), but m also collapses to a value close to 1/2. The form $\rho = \rho_0 \exp (T_0/T)^{1/2}$ is thus robustly adhered to, specifically in the T_A region where structural and chemical characterization reveal the onset of the bulk pyrrhotite minority phase. In light of (a) our prior work demonstrating how readily conductive nanoclusters can induce such hopping conduction in pyrite thin films,[32] (b) the simultaneity of the observation of $\rho = \rho_0 \exp (T_0/T)^{1/2}$ with the onset of a pyrrhotite bulk minority phase, and (c) the known conductive nature of pyrrhotite,[37,46] we conclude that hopping associated with conductive pyrrhotite nanoregions in a more insulating matrix of FeS_2 is active. Careful annealing *time* studies at T_A = 350 °C corroborate this picture. As shown in SI Figure S4, for example, anneals for 1, 24, and 72 h reveal the monotonic growth of a small but detectable $Fe_{1-\delta}S$ minority phase. This consistently results in electronic transport with $m \approx 1/2$, extracted values at these annealing times being 0.49, 0.48, and 0.49, with impressively close adherence to $\rho = \rho_0 \exp (T_0/T)^m$, over the entire measured T range (SI Figure S5). At 350 and 400 °C, five separate samples (in Figure 3 and SI Figure S4) thus result in m values of 0.49, 0.61, 0.49, 0.48, and 0.49, which we take as strong evidence of $m = 1/2$. This conclusion comes from $\rho(T)$ data sets with >2000 points, spanning more than an order of magnitude in T (300 to <20 K) and four decades of resistivity.

It is important to emphasize that comparison of Figures 1 and 2 implies, unsurprisingly, that the reduction of FeS_2 initiates at the surface, and it is thus logical that the significant volume fraction of $Fe_{1-\delta}S$ that emerges around $T_A \approx 350$−400 °C does so in localized regions at the surfaces and grain boundaries of the FeS_2 crystallites. This overall picture is clearly related to the hopping induced by nanoscale unreacted Fe clusters due to inadequate sulfidation in ref 32, but in this case is due to nanoscopic $Fe_{1-\delta}S$ clusters forming upon reduction of FeS_2, likely at the grain interfaces/surface. Even further evidence for these conclusions will be provided below, from magnetic and magnetotransport measurements.

As a final comment on the data shown in Figure 3(b), note that, as expected from Figure 3(a), the Zabrodskii plots at $T_A \geq 425$ °C show ln$W$ decreasing on cooling (Figure 3(b)), indicative of metallic transport. Consistent with this, plots of low temperature conductivity vs T suggest finite conductivity as $T \to 0$ for 425 and 450 °C, implying metallic behavior; at 550 °C the behavior is close to the metal−insulator transition. This overall behavior reflects the emergence of the conductive $Fe_{1-\delta}S$ pyrrhotite majority phase (Figures 1 and 2) with increasing T_A. In the SI (Figure S6), we in fact provide an example of a film that was vacuum annealed under slightly different conditions, resulting in a sufficiently conductive pyrrhotite majority phase that positive $d\rho/dT$ is maintained over a wide T range. This is consistent with the metallic character of pyrrhotite.[37,46]

Further insight is obtained from measurements of the Hall effect, which are shown in Figure 4(a) for an unannealed sample as well as representative T_A values of 250, 350, and 550 °C. The data are presented as Hall resistivity, ρ_{xy} (zero field background subtracted) vs applied magnetic field, H, at 290 K. Again consistent with our prior work,[32] the unannealed FeS_2 film exhibits a robust, field-linear Hall signal, the slope of $\rho_{xy}(H)$ being electron-like (negative). Given that we have clearly demonstrated that hopping transport does *not* occur in this T range in such unannealed samples, this can be definitively ascribed to n-type conduction. Following the simplest analysis results in $n = 5.7 \times 10^{20}$ cm^{-3}, and $\mu = 0.03$ cm^{2}V^{-1}s^{-1} at 290 K. The dopant responsible for the n-type conduction in our case, and the heavy doping level (which is common in pyrite films) remains to be clarified, and is a major open issue in the field. At $T_A = 250$ °C, the Hall coefficient ($R_H = \rho_{xy}/\mu_0 H$) is significantly decreased in magnitude, however, and, at 350 °C, it in fact changes sign to hole-like. This small positive R_H is then maintained as T_A is increased to 550 °C. Vitally, the sign reversal in R_H is coincident *not* with the conversion to a pyrrhotite majority phase and the associated metal−insulator transition ($T_A \approx 425$ °C, Figures 1 and 3), but with the first onset of a bulk pyrrhotite minority phase and the associated crossover to hopping ($T_A \approx 350$ °C, Figure 3(b)). This is therefore clearly the sign-reversal (and suppression) of R_H due to the onset of hopping conduction,[32−35] as discussed in Section 1; it occurs well before the coalescence and percolation of pyrrhotite into a majority phase. That R_H remains positive and relatively small as T_A is further increased, and pyrrhotite begins to dominate, consistent with the established high p-type carrier densities at room temperature in pyrrhotite single crystals.[46] In our case, we obtain $p = 6.5 \times 10^{21}$ cm^{-3} and $\mu = 0.25$ cm^{2}V^{-1}s^{-1} when pyrrhotite dominates, again using the simplest model that assumes one dominant carrier type.

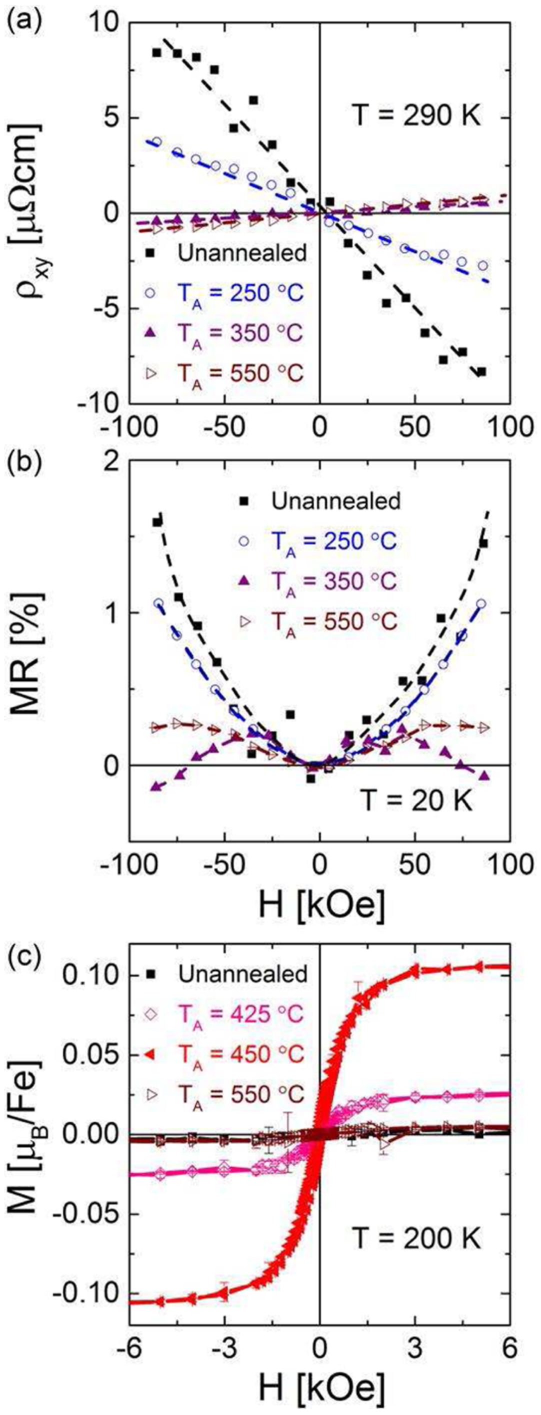

Figure 4. Magnetic field (H) dependence of (a) the zero-field background subtracted Hall resistivity (ρ_{xy}) at 290 K and (b) the magnetoresistance (MR) at 20 K for $Al_2O_3(0001)/FeS_2$ films annealed at 250, 350, and 550 °C. H is applied perpendicular to the plane in all cases, and an unannealed film is shown for comparison. (c) 200 K magnetization hysteresis loops of similar FeS_2 films annealed at 425, 450, and 550 °C. Again, an unannealed film is shown for comparison.

The crossover to hopping transport at $T_A \approx 350$ °C (Figure 3(b)) that is so clearly reflected in the Hall effect (Figure 4(a)) is also evident from magnetoresistance (MR) data. Specifically, as shown in Figure 4(b), the MR ($[(\rho(H) - \rho(0))/\rho(0)] \times 100\%$) in unannealed and 250 °C films is positive and approximately parabolic at a cryogenic temperature of 20 K, amounting to ∼1%. These data are taken with H perpendicular to the film plane (and therefore the current), and the positive quadratic MR thus adheres well to expectations for diffusive/band transport in a nonmagnetic semiconductor. At $T_A = 350$ °C, however, this simple positive MR is replaced with more complex nonmonotonic behavior, a negative contribution emerging at the highest H. This is exactly as seen with decreasing sulfidation temperature in our prior work,[32] and interpreted in terms of magnetism in the conductive nanoclusters (Fe-rich in that case) that induce hopping conduction. In the current case pyrrhotite $Fe_{1-\delta}S$ is also magnetically ordered,[37] and thus this explanation remains relevant.

To further probe the possibility of nontrivial magnetism due to the reduction of FeS_2, magnetization hysteresis loops ($M(H)$) were recorded at 200 K at various important T_A values, as shown in Figure 4(c). The diverse magnetic behaviors of the various constituents of the Fe—S phase diagram render such measurements sensitive to the phases present, potentially even more so than the data of Figure 1. Specifically, FeS_2 is a zero-spin diamagnet[32,37] and Fe is obviously a long-range ordered ferromagnet with a high Curie temperature, while the magnetic ground states of the intermediate Fe sulfides are nontrivial. Briefly, troilite FeS is an antiferromagnet with a Néel temperature near 590 K,[37] whereas pyrrhotite $Fe_{1-\delta}S$ is ferrimagnetic,[37] with magnetization and ordering temperature strongly dependent on δ.[55] At the Fe_7S_8 composition, for instance, a ferrimagnet with an ordering temperature of 580 K has been reported.[37] Examining the 200 K data in Figure 4(c), we first find in the unannealed phase-pure FeS_2 film negligible magnetization, consistent with the expectation of diamagnetic response from phase-pure pyrite. As T_A is increased the situation is unchanged (data not shown) until 425 °C. At this point, clear saturation magnetization turns on (at about 0.025 μ_B/Fe), with a ferromagnetic-like $M(H)$, increasing to 0.1 μ_B/Fe at T_A = 450 °C. This is consistent with Figures 1 and 2, the magnetization being ascribed to the growing volume fraction of ferrimagnetic pyrrhotite. This is a strong indication that the specific $Fe_{1-\delta}S$ phase in this T_A region is close to Fe_7S_8, a suspicion that is backed up by the measurement of a magnetic ordering temperature well above 300 K (SI Figure S7), consistent with the known properties of this phase. Interestingly, as T_A is increased further, to 550 °C, the magnetization drops again, falling to negligible levels. One possible interpretation (consistent with the S/Fe ratio from EDS (Figure 1)) is that the δ in $Fe_{1-\delta}S$ decreases with T_A, reaching $\delta \approx 0$ at 550 °C, i.e., a transformation from ferrimagnetic pyrrhotite Fe_7S_8 toward antiferromagnetic troilite FeS.[55]

3. DISCUSSION AND CONCLUSIONS

The left panel of Figure 5 provides a summary of the main findings of this work. Specifically, Figure 5(a)−(f) shows the T_A dependence of the key quantities extracted from the structural/chemical characterization and transport/magnetic measurements, depicting unannealed films simply at T_A = 0. The panels (a) through (f) plot, respectively, the EDS S/Fe ratio (with the dominant chemical phase labeled above the panel), the resistivity (ρ) at 20 and 300 K, the limiting low T value of the exponent m in $\rho = \rho_0 \exp\,(T_0/T)^m$, the magnitude of the Hall coefficient, R_H (with the sign indicated), the 90 kOe magnetoresistance (MR) value, and the saturation magnetization (M_S) at 200 K. The crossover in primary phase between pyrite FeS_2 and pyrrhotite $Fe_{1-\delta}S$ between 400 and 425 °C is marked by the vertical orange dotted line.

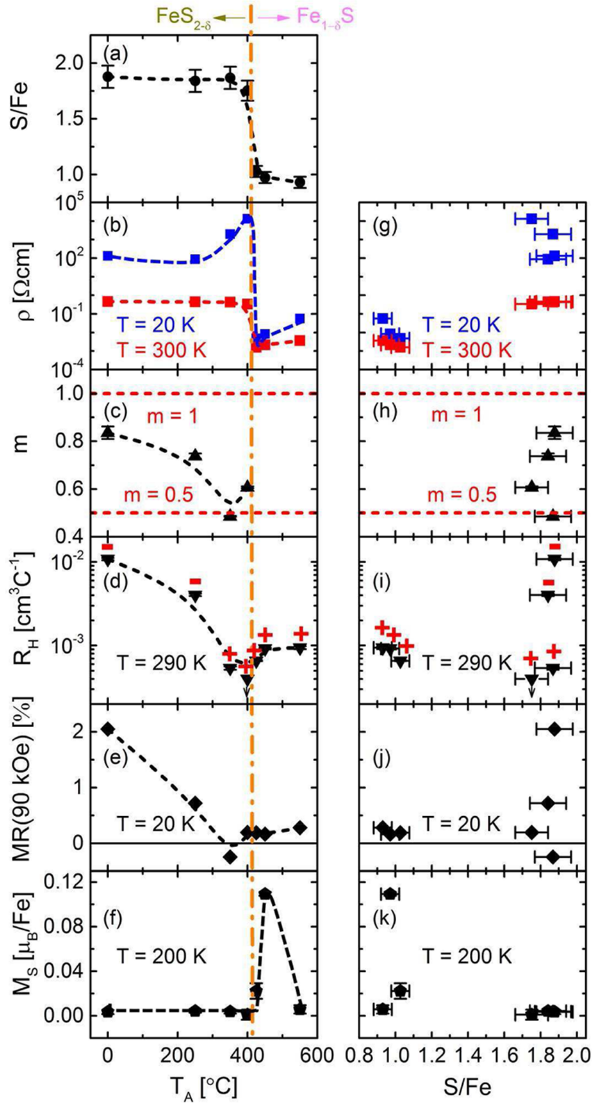

Figure 5. Annealing temperature (T_A) dependence of (a) the S to Fe ratio from energy dispersive spectroscopy, (b) the 20 and 300 K resistivity, ρ, (c) m, the exponent in $\rho = \rho_0 \exp\,(T_0/T)^m$, (d) the magnitude of the 290 K Hall coefficient, R_H, (e) the 20 K magnetoresistance at 90 kOe, and (f) the 200 K saturation magnetization, M_S. Note that T_A = 0 indicates "unannealed". In panel (c), the horizontal dashed lines mark m = 0.5 and 1. In panel (d), the ± symbols indicate the sign of the Hall coefficient, and the arrow represents an upper bound. The vertical orange line indicates the point at which the majority phase converts from pyrite FeS_2 to pyrrhotite $Fe_{1-\delta}S$. The same parameters, ρ, m, R_H, MR(90 kOe), and M_S, are plotted as a function of the S/Fe ratio in panels (g), (h), (i), (j), and (k).

While the overall transformation in majority phase at around 400 °C is abundantly clear from Figure 5(a), a number of other features warrant further discussion and reiteration. The first is the diffusive to hopping transport crossover that takes place prior to the pyrite to pyrrhotite majority phase transformation, i.e., to the left of the dashed vertical line. This crossover is most clearly reflected in the decrease in m in Figure 5(c) to $m \approx 0.5$, but is also reflected more subtly in the resistivity data shown in Figure 2(b), as the upturn in the low T value. This is of course a consequence of the changes in ρ_0, T_0, and m that take place in $\rho = \rho_0 \exp\,(T_0/T)^m$ at the crossover point, i.e., the entry to the hopping regime associated with the pyrrhotite nanocluster minority phase. As already mentioned, the evidence for $m = 1/2$ in the 350−400 °C range is strong, the increase at lower T_A being due to the crossover toward m = 1. As discussed in Section 2.3, this hopping transport also leads to suppression of the magnitude of R_H, in addition to a sign change from negative to positive (Figure 5(d)). We reiterate that this reflects the unambiguously n-type conduction in the unannealed films, crossing over at $T_A \approx 350$ °C to a regime where the sign of R_H is inverted, not due to some unexplained n to p crossover, but to the failure of the Hall effect to accurately reflect the true sign of the charge carriers (Section I). The rise in R_H on further increasing T_A and crossing the vertical dashed line in Figure 5(d) is then due to the onset of the majority pyrrhotite phase, a hole conductor.[37,46] The MR data of Figure 5(e) are consistent, the small positive MR expected from a nonmagnetic semiconductor such as FeS_2 in the diffusive transport regime being replaced with more complex (Figure 4(b)) MR in the hopping regime, even dipping to net negative values in the crossover region (Figure 5(e)). This is ascribed to magnetism in the pyrrhotite nanoclusters that induce the hopping transport. Finally, as shown in Figure 5(f), the magnetic behavior from Figure 4(c) can be summarized by the T_A dependence of the 200 K M_S. This reveals the rapid increase in M_S associated with the ferrimagnetic Fe_7S_8 pyrrhotite phase, followed by the aforementioned decrease, potentially due to antiferromagnetic troilite FeS.

Additional insight is obtained by replotting the data of Figure 5(b)−(f) as a function not of T_A, but rather of the EDS S/Fe ratio (from Figure 5(a)). The result is shown in Figure 5(g)−(k), i.e., the right panel of Figure 5. The most obvious result of this method of presenting the data is clearly the striking clustering of the data points at S/Fe ≈ 1 and S/Fe ≈ 2, underscoring the abrupt nature of the conversion from pyrite to pyrrhotite majority phases with increasing T_A. Discussing panels (g)−(k) in sequence, Figure 5(g) first reflects the large decrease in resistivity that occurs across the MIT, when pyrite FeS_2 is reduced to pyrrhotite FeS. From Figure 5(h), however, the gradual reduction in the exponent m from ∼1.0 to ∼0.5 can be clearly seen, signaling the diffusive to hopping crossover. This is also reflected in Figure 5(i), where, with decreasing S/Fe ratio, a large decrease in the magnitude of R_H and a sign reversal from negative to positive are seen, followed by a jump to S/Fe ≈ 1 and p-type behavior due to majority pyrrhotite. A closely related trend is seen in the MR (Figure 5(j)). Finally, in Figure 5(k) we find $M_S \approx 0$ when S/Fe ≈ 2 (diamagnetic pyrite), growing to $M_S = 0.1$ μ_B/Fe with reducing S/Fe ratio (due to ferrimagnetic pyrrhotite), ultimately returning to $M_S \approx 0$ due to the hypothesized conversion toward troilite FeS.

In summary, a comprehensive study of the evolution in phase stability, stoichiometry, and their impact on electronic transport has been provided in initially phase-pure pyrite FeS_2 films subject to vacuum annealing at increasing temperatures. Bulk and surface structural and chemical characterization, on both polycrystalline films and 001-oriented crystals, reveals formation of a pyrrhotite $Fe_{1-\delta}S$ minority phase at temperatures as low as 160 °C (likely confined to the surface), followed by clearer growth at 400 °C, and then rapid transformation to a $Fe_{1-\delta}S$ majority phase by 425 °C. This induces a sequence of changes in the electronic transport, first from a diffusive to hopping transport, and then from strongly semiconducting to metallic. The first of these is driven by hopping in the presence of nanoscale conductive clusters of $Fe_{1-\delta}S$, the second by an MIT due to the majority phase $Fe_{1-\delta}S$. The crossover from diffusive to hopping transport leads to a large decrease in magnitude, and sign reversal, in the Hall coefficient, underscoring the need to properly understand the conduction mechanism in order to determine the sign of the dominant charge carriers in pyrite films. Careful analysis of additional data, such as magnetoresistance and magnetization, provide equally detailed information on the sequence of phase transformations that occur upon reduction.

These data and conclusions significantly clarify important issues regarding phase stability, phase purity, secondary phase formation, stoichiometry, doping, and transport in pyrite. First and foremost, while the minority phase formation is clearly an important issue in FeS_2 films (particularly at the nanoscale), phase-pure pyrite films are certainly possible, within the detection limits of the techniques applied.[56] Ex situ sulfidation is apparently capable of this, although the resulting high densities of uncontrolled dopants, and associated low mobilities, must be mitigated in future work. On the basis of the results in this paper, postsynthesis annealing (at least in the absence of significant S vapor pressure) is not promising for this defect mitigation. Thermal treatment under reducing conditions in fact leads not to some window where S vacancy concentration can be controlled in $FeS_{2-\delta}$ (at least at these high carrier densities; further work with low electron density crystals is worthwhile), but rather to the facile formation of pyrrhotite $Fe_{1-\delta}S$ minority phases. These occur first at the surface, followed by the grain boundaries, and eventually through the bulk. The detected sequence of phases with vacuum annealing is concluded to be FeS_2 (pyrite), Fe_7S_8 (pyrrhotite), and then FeS (troilite). No marcasite FeS_2 or greigite Fe_3S_4 were detected, within the limits of the techniques used. In terms of additional impact on electronic transport, the findings in this work inform future FeS_2-based solar cell device development in two specific ways: significant attention must be paid to mitigating local S/Fe variations in order to obtain diffusive band transport, and clear evidence of such should be obtained in order to reliably determine the majority carrier type.

4. EXPERIMENTAL SECTION

Polycrystalline FeS_2 films were fabricated by ex situ sulfidation. In the first step, 33 nm thick (from grazing incidence X-ray reflectivity) Fe films were deposited on large (approximately 50 × 4 mm^2) chemically cleaned $Al_2O_3(0001)$ substrates via DC magnetron sputtering (base pressure typically $<1 \times 10^{-8}$ Torr) from an Fe target (Kurt J. Lesker, 99.9% purity). An Ar pressure of 2.3 mTorr and a substrate temperature of 300 °C were used, resulting in a deposition rate of 0.08 nm/s and (110) out-of-plane texture. The Fe films were then placed in an evacuated (10^{-6} Torr) and sealed quartz ampule (8 cm^3) with 1.0 ± 0.1 mg of S (CERAC, 99.999% purity) and sulfidized. Heating took place at 6.5 °C/min, followed by isothermal sulfidation at 600 °C for 8 h (estimated S pressure 35 Torr) followed by furnace cooling. Care was taken to avoid S condensation on the film during cooling.

As-made FeS_2 films were then fractured into multiple pieces (approximately 4 × 4 mm^2) for WAXRD, SEM/EDS, Raman spectroscopy, electronic transport, and magnetometry. Vacuum annealing of these films was performed at a single temperature (T_A), between 250 and 550 °C, for 1 h, in a chamber with a base pressure $\sim 1 \times 10^{-6}$ Torr. WAXRD data were then collected with a Bruker-AXS PLATFORM X-ray diffractometer equipped with a Cu source, a graphite monochromator ($K\alpha$ pass-through filter), a 0.8 mm incident beam point collimator, and a 2D Hi-Star area detector. Microstructure and composition were examined using a JEOL 6500F field emission SEM with a Thermo-Noran Vantage EDS system, and Raman data were collected in the backscattering geometry using a WiTec alpha300R confocal microscope equipped with a UHTS 300 spectrometer and a DV401 CCD detector. Temperature- and field-dependent transport measurements (5−300 K) were made in a Janis cryostat and/or a Quantum Design Physical Property Measurement System (PPMS), both equipped with 90 kOe superconducting magnets. Soldered indium contacts in a van der Pauw configuration were employed, using AC (13.7 Hz) and DC excitation, depending on the magnitude of the resistance. Extensive checks for ohmicity, excessive contact resistance, and self-heating were made. Hall measurements were done AC (with a resistance bridge), paying particular attention to temperature stability. Magnetometry was done in a Quantum Design Superconducting Quantum Interference Device (SQUID) magnetometer from 5 to 300 K in fields up to 70 kOe.

Single crystals of FeS_2 were grown via a chemical vapor transport (CVT) method (see refs 15 and 41, and references therein), in which FeS_2 (Alfa Aesar, 99.9% purity) and S (CERAC, 99.999% purity) were employed as source materials, with $FeBr_2$ (Sigma-Aldrich, 99.999% purity) as a transport agent. Briefly, 2.2 g of FeS_2 powder, 100 mg of $FeBr_2$ powder, and 580 mg of S powder were loaded into an evacuated (10^{-6} Torr) and sealed quartz ampule (52 cm^3) in a two-zone tube furnace. The source materials were loaded into the "source zone", crystals nucleating in the "growth zone". The temperatures of the source and growth zones were first (for the initial 72 h) set at 700 and 730 °C, respectively, i.e., with the growth zone *hotter* than the source zone. This is an approach frequently used in CVT,[41] designed to establish an equilibrium vapor state, and to help "clean" the growth zone of excess potential nucleation sites. CVT growth was then initiated by reversing the temperature gradient, setting the source and growth zones to 670 and 590 °C, respectively. This was maintained for 3 weeks typically, resulting in pyrite single crystals with up to 5 mm wide facets. Phase purity was established with X-ray powder diffraction (with a Bruker-AXS D5005 Diffractometer on powdered crystals) and Raman spectroscopy. Chemical composition was confirmed using EDS, while single crystallinity was confirmed by X-ray diffraction with a 2D area detector (on the same Bruker system described above). Characterization results are provided in SI Figures S2 and S3.

Core level XPS was done on several FeS_2 single crystals in a PHI Versa Probe II system with a monochromatic Al Kα anode X-ray source ($h\nu$ = 1486.6 eV) and a hemispherical analyzer. Measurements were carried out in ultrahigh vacuum (UHV, around 8×10^{-10} Torr), annealing being done with a temperature cycle that involved warm-up in ∼10 min, ∼10 min of equilibration, and cool-down in ∼10 min. As discussed in Section 2.2, standard Ar ion sputter/anneal procedures[22] were avoided. All spectra were recorded using the PHI software package SmartSoft−XPS v2.0 and processed using PHI MultiPack v9.0 and/or CASA XPS v.2.3.14. The positions of the S $2p_{3/2}$ and $2p_{1/2}$ peaks for $Fe_{1-\delta}S$ and $FeS_{2-\delta}$ were identified based on prior literature;[21,22,42] the $2p_{3/2}$ and $2p_{1/2}$ states have an energy spacing of about 1.1 eV, and an intensity ratio of 2.[42] Peaks were fitted using GL line shapes (a widely used hybrid of Gaussian and Lorentzian[57]), with Shirley background subtraction.[58,59] Up to 50 scans were accumulated and averaged to improve the signal-to-noise ratio for each spectrum. The samples were also examined at 5−6 locations, establishing reproducibility. Note that under the conditions used here, XPS is expected to probe no more than 2−5 unit cells. This is supported by angle-resolved data, which indicate that more than 50% of the signal comes from the top 1.5 nm.

■ ASSOCIATED CONTENT

Ⓢ Supporting Information

Additional structural, chemical, electronic, and magnetometry measurement results. The Supporting Information is available free of charge on the ACS Publications website at DOI: 10.1021/acsami.5b03422.

■ AUTHOR INFORMATION

Corresponding Authors

*E-mail: aydil@umn.edu (E.S.A.).
*E-mail: leighton@umn.edu (C.L.).

Notes

The authors declare no competing financial interest.

■ ACKNOWLEDGMENTS

Numerous illuminating discussions with B.I. Shklovskii on hopping conduction are acknowledged. This work was supported by the U.S. National Science Foundation (NSF) through DMR-1309642. Additional support acknowledged from the UMN NSF MRSEC under DMR-0819885 and DMR-1420013, as well as UMN IREE. X.Z. gratefully acknowledges a UMN Doctoral Dissertation Fellowship. Parts of the work carried out in the UMN Characterization Facility, which receives partial support from the MRSEC program. Work at UNL supported by C-SPIN, part of STARnet, an SRC program sponsored by MARCO and DARPA (SRC 2381.003), as well as the NSF-funded UNL MRSEC (DMR-1420645). Access to the XPS at the IU Nanoscale Characterization Facility was provided by NSF through DMR MRI-1126394.

■ REFERENCES

(1) Ennaoui, A.; Fiechter, S.; Pettenkofer, C.; Alonso-Vante, N.; Büker, K.; Bronold, M.; Höpfner, C.; Tributsch, H. Iron Disulfide for Solar Energy Conversion. *Sol. Energy Mater. Sol. Cells* **1993**, *29*, 289−370.

(2) Wolden, C. A.; Kurtin, J.; Baxter, J. B.; Repins, I.; Shaheen, S. E.; Torvik, J. T.; Rockett, A. A.; Fthenakis, V. M.; Aydil, E. S. Photovoltaic Manufacturing: Present Status, Future Prospects, and Research Needs. *J. Vac. Sci. Technol. A* **2011**, *29*, 030801.

(3) Wadia, C.; Alivisatos, A. P.; Kammen, D. M. Materials Availability Expands the Opportunity for Large-Scale Photovoltaics Deployment. *Environ. Sci. Technol.* **2009**, *43*, 2072−2077.

(4) Morrish, R.; Silverstein, R.; Wolden, C. A. Synthesis of Stoichiometric FeS_2 through Plasma-Assisted Sulfurization of Fe_2O_3 Nanorods. *J. Am. Chem. Soc.* **2012**, *134*, 17854−17857.

(5) Berry, N.; Cheng, M.; Perkins, C. L.; Limpinsel, M.; Hemminger, J. C.; Law, M. Atmospheric-Pressure Chemical Vapor Deposition of Iron Pyrite Thin Films. *Adv. Energy Mater.* **2012**, *2*, 1124−1135.

(6) Seefeld, S.; Limpinsel, M.; Liu, Y.; Farhi, N.; Weber, A.; Zhang, Y.; Berry, N.; Kwon, Y. J.; Perkins, C. L.; Hemminger, J. C.; Wu, R.; Law, M. Iron Pyrite Thin Films Synthesized from an $Fe(acac)_3$ Ink. *J. Am. Chem. Soc.* **2013**, *135*, 4412−4424.

(7) Sentman, C. D.; O'Brien, M.; Wolden, C. A. Self Limiting Deposition of Pyrite Absorbers by Pulsed PECVD. *J. Vac. Sci. Technol. A* **2014**, *32*, 021201.

(8) Baruth, A.; Manno, M.; Narasimhan, D.; Shankar, A.; Zhang, X.; Johnson, M.; Aydil, E. S.; Leighton, C. Reactive Sputter Deposition of Pyrite Structure Transition Metal Disulfide Thin Films: Microstructure, Transport, and Magnetism. *J. Appl. Phys.* **2012**, *112*, 054328.

(9) Puthussery, J.; Seefeld, S.; Berry, N.; Gibbs, M.; Law, M. Colloidal Iron Pyrite (FeS_2) Nanocrystal Inks for Thin-Film Photovoltaics. *J. Am. Chem. Soc.* **2011**, *133*, 716−719.

(10) Bi, Y.; Yuan, Y.; Exstrom, C. L.; Darveau, S. A.; Huang, J. Air Stable, Photosensitive, Phase Pure Iron Pyrite Nanocrystal Thin Films for Photovoltaic Application. *Nano Lett.* **2011**, *11*, 4953−4957.

(11) Cabán-Acevedo, M.; Faber, M. S.; Tan, Y.; Hamers, R. J.; Jin, S. Synthesis and Properties of Semiconducting Iron Pyrite (FeS_2) Nanowires. *Nano Lett.* **2012**, *12*, 1977−1982.

(12) Lucas, J. M.; Tuan, C.-C.; Lounis, S. D.; Britt, D. K.; Qiao, R.; Yang, W.; Lanzara, A.; Alivisatos, A. P. Ligand-Controlled Colloidal Synthesis and Electronic Structure Characterization of Cubic Iron Pyrite (FeS_2) Nanocrystals. *Chem. Mater.* **2013**, *25*, 1615−1620.

(13) Cabán-Acevedo, M.; Liang, D.; Chew, K. S.; DeGrave, J. P.; Kaiser, N. S.; Jin, S. Synthesis, Characterization, and Variable Range Hopping Transport of Pyrite (FeS_2) Nanorods, Nanobelts, and Nanoplates. *ACS Nano* **2013**, *7*, 1731−1739.

(14) Limpinsel, M.; Farhi, N.; Berry, N.; Lindemuth, J.; Perkins, C. L.; Lin, Q.; Law, M. An Inversion Layer at the Surface of N-Type Iron Pyrite. *Energy Environ. Sci.* **2014**, *7*, 1974−1989.

(15) Cabán-Acevedo, M.; Kaiser, N. S.; English, C. R.; Liang, D.; Thompson, B. J.; Chen, H.-E.; Czech, K. J.; Wright, J. C.; Hamers, R. J.; Jin, S. Ionization of High-Density Deep Donor Defect States Explains the Low Photovoltage of Iron Pyrite Single Crystals. *J. Am. Chem. Soc.* **2014**, *136*, 17163−17179.

(16) Yu, L.; Lany, S.; Kykyneshi, R.; Jieratum, V.; Ravichandran, R.; Pelatt, B.; Altschul, E.; Platt, H. A. S.; Wager, J. F.; Keszler, D. A.; Zunger, A. Iron Chalcogenide Photovoltaic Absorbers. *Adv. Energy Mater.* **2011**, *1*, 748−753.

(17) Sun, R.; Chan, M. K. Y.; Kang, S.; Ceder, G. Intrinsic Stoichiometry and Oxygen-Induced p-Type Conductivity of Pyrite FeS_2. *Phys. Rev. B* **2011**, *84*, 035212.

(18) Hu, J.; Zhang, Y.; Law, M.; Wu, R. First-Principles Studies of the Electronic Properties of Native and Substitutional Anionic Defects in Bulk Iron Pyrite. *Phys. Rev. B* **2012**, *85*, 085203.

(19) Sun, R.; Chan, M. K. Y.; Ceder, G. First-Principles Electronic Structure and Relative Stability of Pyrite and Marcasite: Implications for Photovoltaic Performance. *Phys. Rev. B* **2011**, *83*, 235311.

(20) Zhang, Y. N.; Hu, J.; Law, M.; Wu, R. Q. Effect of Surface Stoichiometry on the Band Gap of the Pyrite FeS_2(100) Surface. *Phys. Rev. B* **2012**, *85*, 085314.

(21) Herbert, F. W.; Krishnamoorthy, A.; Ma, W.; Van Vliet, K. J.; Yildiz, B. Dynamics of Point Defect Formation, Clustering and Pit Initiation on the Pyrite Surface. *Electrochim. Acta* **2014**, *127*, 416−426.

(22) Andersson, K. J.; Ogasawara, H.; Nordlund, D.; Brown, G. E.; Nilsson, A. Preparation, Structure, and Orientation of Pyrite FeS_2 {100} Surfaces: Anisotropy, Sulfur Monomers, Dimer Vacancies, and a Possible FeS Surface Phase. *J. Phys. Chem. C* **2014**, *118*, 21896−21903.

(23) Steinhagen, C.; Harvey, T. B.; Stolle, C. J.; Harris, J.; Korgel, B. A. Pyrite Nanocrystal Solar Cells: Promising, or Fool's Gold? *J. Phys. Chem. Lett.* **2012**, *3*, 2352−2356.

(24) Büker, K.; Alonso-Vante, N.; Tributsch, H. Photovoltaic Output Limitation of n-FeS_2 (pyrite) Schottky Barriers: A Temperature-Dependent Characterization. *J. Appl. Phys.* **1992**, *72*, 5721−5728.

(25) Liang, D.; Cabán-Acevedo, M.; Kaiser, N. S.; Jin, S. Gated Hall Effect of Nanoplate Devices Reveals Surface-State-Induced Surface Inversion in Iron Pyrite Semiconductor. *Nano Lett.* **2014**, *14*, 6754−6760.

(26) Herbert, F. W.; Krishnamoorthy, A.; Van Vliet, K. J.; Yildiz, B. Quantification of Electronic Band Gap and Surface States on FeS_2(100). *Surf. Sci.* **2013**, *618*, 53−61.

(27) Schieck, R.; Hartmann, A.; Fiechter, S.; Könenkamp, R.; Wetzel, H. Electrical Properties of Natural and Synthetic Pyrite (FeS_2) Crystals. *J. Mater. Res.* **1990**, *5*, 1567−1572.

(28) Yamamoto, A.; Nakamura, M.; Seki, A.; Li, E. L.; Hashimoto, A.; Nakamura, S. Pyrite (FeS_2) Thin Films Prepared by Spray Method Using $FeSO_4$ and $(NH_4)_2S_x$. *Sol. Energy Mater. Sol. Cells* **2003**, *75*, 451−456.

(29) Willeke, G.; Dasbach, R.; Sailer, B.; Bucher, E. Thin Pyrite (FeS_2) Films Prepared by Magnetron Sputtering. *Thin Solid Films* **1992**, *213*, 271−276.

(30) Lichtenberger, D.; Ellmer, K.; Schieck, R.; Fiechter, S.; Tributsch, H. Structural, Optical and Electrical Properties of Polycrystalline Iron Pyrite Layers Deposited by Reactive d.c. Magnetron Sputtering. *Thin Solid Films* **1994**, *246*, 6−12.

(31) Soukup, R. J.; Prabukanthan, P.; Ianno, N. J.; Sarkar, A.; Kamler, C. A.; Sekora, D. G. Formation of Pyrite (FeS_2) Thin Films by Thermal Sulfurization of dc Magnetron Sputtered Iron. *J. Vac. Sci. Technol. A* **2011**, *29*, 011001.

(32) Zhang, X.; Manno, M.; Baruth, A.; Johnson, M.; Aydil, E. S.; Leighton, C. Crossover From Nanoscopic Intergranular Hopping to Conventional Charge Transport in Pyrite Thin Films. *ACS Nano* **2013**, *7*, 2781−2789.

(33) Le Comber, P. G.; Jones, D. I.; Spear, W. E. Hall Effect and Impurity Conduction in Substitutionally Doped Amorphous Silicon. *Philos. Mag.* **1977**, *35*, 1173−1187.

(34) Galperin, Y. M.; German, E. P.; Karpov, V. G. Hall Effect under Hopping Conduction Conditions. *Sov. Phys. JETP* **1991**, *72*, 193−200.

(35) Kakalios, J. A Physical Interpretation of the Hall Effect in Amorphous Semiconductors. *J. Non-Cryst. Solids* **1989**, *114*, 372−374.

(36) Birkholz, M.; Fiechter, S.; Hartmann, A.; Tributsch, H. Sulfur Deficiency in Iron Pyrite (FeS_{2-X}) and Its Consequences for Band-Structure Models. *Phys. Rev. B* **1991**, *43*, 11926−11936.

(37) Vaughan, D. J.; Craig, J. R. *Mineral Chemistry of Metal Sulfides*; Cambridge University Press: Cambridge/New York, 1978.

(38) PDF#00-042-1340.

(39) PDF#00-024-0220.

(40) Mernagh, T. P.; Trudu, A. G. A Laser Raman Microprobe Study of Some Geologically Important Sulphide Minerals. *Chem. Geol.* **1993**, *103*, 113−127.

(41) Wang, L.; Chen, T. Y.; Chien, C. L.; Leighton, C. Sulfur Stoichiometry Effects in Highly Spin Polarized CoS_2 Single Crystals. *Appl. Phys. Lett.* **2006**, *88*, 232509.

(42) Knipe, S. W.; Mycroft, J. R.; Pratt, A. R.; Nesbitt, H. W.; Bancroft, G. M. X-Ray Photoelectron Spectroscopic Study of Water Adsorption on Iron Sulphide Minerals. *Geochim. Cosmochim. Acta* **1995**, *59*, 1079−1090.

(43) De Donato, P.; Mustin, C.; Benoit, R.; Erre, R. Spatial Distribution of Iron and Sulphur Species on the Surface of Pyrite. *Appl. Surf. Sci.* **1993**, *68*, 81−93.

(44) Brion, D. Etude Par Spectroscopie de Photoélectrons de La Dégradation Superficielle de FeS_2, $CuFeS_2$, ZnS et PbS À L'air et Dans L'eau. *Appl. Surf. Sci.* **1980**, *5*, 133−152.

(45) Moulder, J. F.; Stickle, W. F.; Sobol, P. E.; Bomben, K. D. *Handbook of X-Ray Photoelectron Spectroscopy*; Physical Electronics: Eden Prairie, MN, 1993.

(46) Theodossiou, A. Measurements of the Hall Effect and Resistivity in Pyrrhotite. *Phys. Rev.* **1965**, *137*, A1321−A1326.

(47) Zabrodskii, A. G. The Coulomb Gap: The View of an Experimenter. *Philos. Mag. Part B* **2001**, *81*, 1131−1151.

(48) Shklovskii, B. I.; Efros, A. L. *Electronic Properties of Doped Semiconductors*; Springer Series in Solid-State Sciences; Springer-Verlag: Berlin; New York, 1984.

(49) Mott, N. *Metal-Insulator Transitions*, 2^{nd} ed.; CRC Press: London/New York, 1990.

(50) Sheng, P.; Abeles, B.; Arie, Y. Hopping Conductivity in Granular Metals. *Phys. Rev. Lett.* **1973**, *31*, 44−47.

(51) Abeles, B.; Sheng, P.; Coutts, M. D.; Arie, Y. Structural and Electrical Properties of Granular Metal Films. *Adv. Phys.* **1975**, *24*, 407−461.

(52) Pollak, M.; Adkins, C. J. Conduction in Granular Metals. *Philos. Mag. B* **1992**, *65*, 855−860.

(53) Zhang, J.; Shklovskii, B. I. Density of States and Conductivity of a Granular Metal or an Array of Quantum Dots. *Phys. Rev. B* **2004**, *70*, 115317.

(54) Beloborodov, I. S.; Lopatin, A. V.; Vinokur, V. M.; Efetov, K. B. Granular Electronic Systems. *Rev. Mod. Phys.* **2007**, *79*, 469−518.

(55) Takayama, T.; Takagi, H. Phase-Change Magnetic Memory Effect in Cation-Deficient Iron Sulfide $Fe_{1-x}S$. *Appl. Phys. Lett.* **2006**, *88*, 012512.

(56) At least with respect to ferromagnetic impurities, magnetometry measurements, here and in ref 32, place quite stringent limits on secondary phase fractions. We estimate them to lie at <0.1 vol. % for the sulfidation temperatures used here (600 °C).

(57) Egelhoff, W. F., Jr. Core-Level Binding-Energy Shifts at Surfaces and in Solids. *Surf. Sci. Rep.* **1987**, *6*, 253−415.

(58) Shirley, D. A. High-Resolution X-Ray Photoemission Spectrum of the Valence Bands of Gold. *Phys. Rev. B* **1972**, *5*, 4709−4714.

(59) Végh, J. The Shirley Background Revised. *J. Electron Spectrosc. Relat. Phenom.* **2006**, *151*, 159−164.